Near-Field MIMO Communication Links

Sendy Phang, Michel T. Ivrlač, *Member, IEEE*, Gabriele Gradoni, *Member, IEEE*, Stephen C. Creagh,
Gregor Tanner, and Josef A. Nossek, *Life Fellow, IEEE*

***Abstract*— A procedure to achieve near-field multiple input multiple output (MIMO) communication with equally strong channels is demonstrated in this paper. This has applications in near-field wireless communications, such as Chip-to-Chip (C2C) communication or wireless links between printed circuit boards. Designing the architecture of these wireless C2C networks is, however, based on standard engineering design tools. To attain this goal, a network optimization procedure is proposed, which introduces decoupling and matching networks. As a demonstration, this optimization procedure is applied to a 2-by-2 MIMO with dipole antennas. The potential benefits and design trade-offs are discussed for implementation of wireless radio-frequency interconnects in chip-to-chip or device-to-device communication such as in an Internet-of-Things scenario.**

***Index Terms*— Impedance matching, antenna arrays, MIMO, device-to-device communication, mutual coupling, near field communication.**

I. INTRODUCTION

TO PERFORM their task, modern devices are equipped with a computing processing unit (CPU) which is connected to various components, such as sensors, memory, actuators, and so forth [1]. This high level of integration leads to increasingly complex circuits and interconnect designs. The latter is a leading data rate bottleneck in improving overall performance. Even though wired electrical interconnects have been shown to be reliable and cheap, complex line designs and device miniaturisation has pushed the capability of electrical interconnects to its very limits [2]–[4]. Alternatives such as optical [2], [3], [5] and RF/wireless interconnects [6] have been proposed. While optical interconnects may provide higher bit-rates, this option may not be as attractive for application in harsh and weight/space constrained environments. In this setting, RF/microwave interconnects offer a promising alternative; it is a matured technology, which has been used in telecommunication ranging from satellite applications to mobile communication and wireless LAN and from long to short ranges. The design process for such RF interconnects is, however, a non-trivial procedure. As these devices have become more compact and better connected, the conventional design procedure for "far-field" communication is no-longer appropriate because antenna elements may be placed in close proximity to each other and strong interaction alters the designed operational state. These challenges motivate the recently assembled European Future Emerging Technology (FET) consortium NEMF21 [7] to plan for a new technological platform for wireless chip-to-chip and device-to-device communication.

An optical wireless interconnect technology based on free-space optics has been proposed [8]–[10]. Implementation of such a system *but* based on Radio-Frequency (RF) in small scale, for application of chip-to-chip or board-to-board communication, is still challenging due to the demand of high data rates and small antenna size with high-efficiency [6]. Different antenna topologies and artificial materials have been proposed to enhance the performance of RF based interconnects [6], [11]–[14]. Little work has been done in investigating the prospect of Multiple-input Multiple-Output (MIMO) technologies to improve the performance of wireless RF interconnects in the near-field. MIMO systems, in which several antennas are used both as transmitters and receivers, have been commonly used to increase the capacity in mobile communication [15]–[17]. Furthermore it is important to note that in the near-field region, the electromagnetic fields are reactive. This characteristic prevents directional EM propagation by beam-forming techniques which have been commonly used in multi-antenna broadcasting by judiciously balancing the phase contributions of transmitter antennas to shape the far-field radiation in space and frequency.

In this paper we present a design approach whose aim is to establish multi-channel communication between a transmit and a receive array in their mutual near-field (see Fig. 1). The approach used in this paper is based on multiport communication theory [18], [19] which provides a natural link between electromagnetic (EM) and information theory frameworks. The multiport communication theory approach has been used in a variety of applications [20]–[27], but always assuming far-field coupling between transmit and receiving arrays. In this paper, we show that to fully exploit the MIMO structure, it is advantageous to introduce Decoupling and Matching

---

Manuscript received August 31, 2017; revised November 12, 2017 and January 11, 2018; accepted January 18, 2018. Date of publication February 12, 2018; date of current version August 3, 2018. This work was supported by the European Commission for NEMF21 project through the framework Horizon 2020 Future Emerging Technologies under Grant 664828. This paper was recommended by Associate Editor H. Johansson. *(Corresponding author: Sendy Phang.)*

S. Phang, S. C. Creagh, and G. Tanner are with the School of Mathematical Sciences, University of Nottingham, Nottingham NG7 2RD, U.K. (e-mail: sendy.phang@nottingham.ac.uk; stephen.creagh@nottingham.ac.uk; gregor.tanner@nottingham.ac.uk).

M. T. Ivrlač is with the Institute for Circuit Theory and Signal Processing, Technische Universität München, 80333 München, Germany (e-mail: ivrlac@tum.de).

G. Gradoni is with the School of Mathematical Sciences, George Green Institute for Electromagnetics Research, University of Nottingham, Nottingham NG7 2RD, U.K. (e-mail: gabriele.gradoni@nottingham.ac.uk).

J. A. Nossek is with the Department of Teleinformatic Engineering, Federal University of Ceará, Fortaleza 60020-181, Brazil, and also with the Institute for Circuit Theory and Signal Processing, Technische Universität München, 80333 München, Germany (e-mail: josef.a.nossek@tum.de).

Color versions of one or more of the figures in this paper are available online at http://ieeexplore.ieee.org.

Digital Object Identifier 10.1109/TCSI.2018.2796305

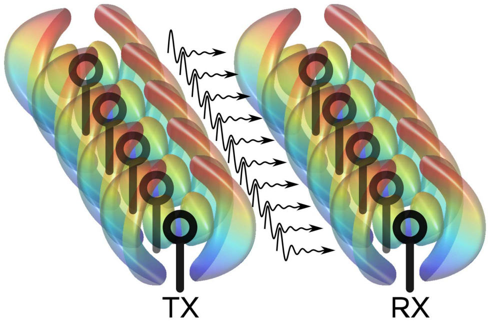

Fig. 1. Schematic illustration of $L \times L$ transmitter and receiver MIMO system.

Networks (DMNs) at both ends of the link in order to achieve maximum power transfer from the transmit to the receive side. For far-field coupling, such as in mobile communication, these DMNs can be designed independently for both sides, as unilateral approximation is applicable. However, for near-field MIMO considered here, the matching condition has to be achieved jointly, which adds a layer of complexity.

We start in Sec. II-A by deriving the power-matching condition for the near-field coupled case. In Sec. II-B, we identify the power gain of the individual communication channels and find conditions leading to equally strong channels. Finally, to demonstrate the applicability of the proposed method, we carry out the optimization procedure explicitly for 2×2 half-wavelength dipole antenna systems in Sec. III. We provide in particular a detailed analysis identifying the existence of two equally strong orthogonal communication channels in the near-field region in Sec. III-A. We study the robustness of this communication scheme in the presence of perturbations due to small differences in the antennas, for example, fabrication tolerances in Sec III-B. We compare the analytical results obtained from assuming idealised dipoles with full-vectorial (Finite-Difference Time-Domain) FDTD calculations in Sec. III-C. This confirms the main findings but also highlights important deviations from the idealised case.

II. NEAR-FIELD MIMO COMMUNICATION

We consider a MIMO communication system with L transmitting antennas (each being independently driven by a signal-generator) and L receiving antennas at near-field separation distances between the antenna arrays, as shown schematically in Fig. 1. The MIMO antenna system can be modelled by an impedance matrix as,

$$\begin{bmatrix} \mathbf{u}_{\mathrm{t}} \\ \mathbf{u}_{\mathrm{r}} \end{bmatrix} = \begin{bmatrix} \mathbf{Z}_{11} & \mathbf{Z}_{12} \\ \mathbf{Z}_{21} & \mathbf{Z}_{22} \end{bmatrix} \begin{bmatrix} \mathbf{i}_{\mathrm{t}} \\ \mathbf{i}_{\mathrm{r}} \end{bmatrix}. \tag{1}$$

Here, the vectors $\mathbf{u}_{\mathrm{t,r}}$ and $\mathbf{i}_{\mathrm{t,r}}$ denote the partitioned voltages and currents at the L transmitter and L receiver ports, respectively. The matrix entries $\mathbf{Z}_{ij}$ with $i, j \in \{1, 2\}$ are four $L \times L$ matrices which make the full $2L \times 2L$ complex impedance matrix $\mathbf{Z}$. The impedance parameters between antenna elements can be obtained numerically or experimentally.

As these antenna elements are positioned within their mutual near-field region, we have the case of a strongly coupled problem. Such strong interaction makes the matching problems on the transmit and the receive sides coupled, which is in contrast to the usual far-field situation.

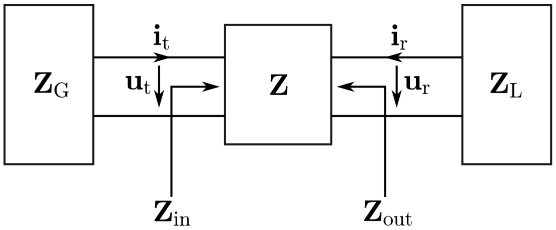

Fig. 2. A block diagram of a linear multi-port antenna system $\mathbf{Z}$ with multiport generator impedance $\mathbf{Z}_{\mathrm{G}}$ attached to the transmit-side of the antenna and a multiport load impedance $\mathbf{Z}_{\mathrm{L}}$ on the receiver-side.

A. Decoupling and Matching Networks (DMNs)

During operation, the antenna system is terminated by a multiport load and driven by a multiport generator; these elements are represented by the impedance matrices $\mathbf{Z}_{\mathrm{L}}$ and $\mathbf{Z}_{\mathrm{G}}$, respectively, as schematically illustrated in Fig. 2. When the generators are switched off, we have

$$\mathbf{u}_{\mathrm{t}} = -\mathbf{Z}_{\mathrm{G}}\mathbf{i}_{\mathrm{t}}, \quad \mathbf{u}_{\mathrm{r}} = -\mathbf{Z}_{\mathrm{L}}\mathbf{i}_{\mathrm{r}}. \tag{2}$$

Therefore, to maximize the power transfer between the transmitter-side and receiver-side, the network should be impedance-matched [28]. That is, we implement a power matching condition (*condition 1*),

$$\mathbf{Z}_{\mathrm{in}} = \mathbf{Z}_{\mathrm{G}}^{\dagger} \text{ and } \mathbf{Z}_{\mathrm{out}} = \mathbf{Z}_{\mathrm{L}}^{\dagger}, \tag{3}$$

where † denotes Hermitian conjugation and $\mathbf{Z}_{\mathrm{in/out}}$ are the input or output impedance parameters from the generator and load sides, as shown in Fig. 2. Upon substituting (2) and (3) into (1), the input and output impedances are related by

$$\begin{aligned} \mathbf{Z}_{\mathrm{G}}^{\dagger} &= \mathbf{Z}_{11} - \mathbf{Z}_{12}(\mathbf{Z}_{22} + \mathbf{Z}_{\mathrm{L}})^{-1}\mathbf{Z}_{21} \\ \mathbf{Z}_{\mathrm{L}}^{\dagger} &= \mathbf{Z}_{22} - \mathbf{Z}_{21}(\mathbf{Z}_{11} + \mathbf{Z}_{\mathrm{G}})^{-1}\mathbf{Z}_{12}. \end{aligned} \tag{4}$$

The relation (4) is a coupled transcendental equation which can be solved by a numerical scheme (Appendix A).

Equations (4) give the input and output impedances to achieve an optimum transmit-received power. In practice, the system will be driven by L independent generators; thus to attain the given generator impedance $\mathbf{Z}_{\mathrm{G}}$ we introduce a Matching network on the Transmitter side (MT) with the impedance parameter denoted by $\mathbf{Z}^{\mathrm{MT}}$ (see Fig. 3). This means that the implementation of $\mathbf{Z}^{\mathrm{MT}}$ requires the overall port impedance on the right-hand side of the generator to equal the generator resistance R, see Fig. 3. That is, we impose the *decoupling* condition (*condition 2*),

$$\mathbf{u}_1 = R\mathbf{I}\mathbf{i}_1, \tag{5}$$

where $\mathbf{I}$ denotes an identity matrix of size $L \times L$. Equation (5) emphasises that the voltages at the left-hand side of the $\mathbf{Z}^{\mathrm{MT}}$ network are *not* coupled, so that the system can be driven by L independent generators (see Fig. 3). This intermediary network serves as a Decoupling and Matching Network (DMN) for the transmitter-side.

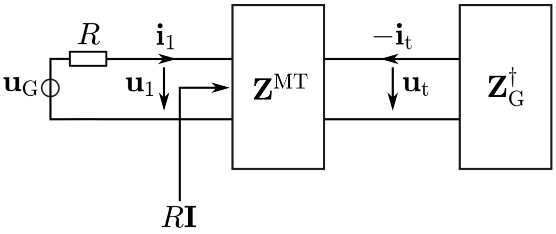

Fig. 3. Block diagram of lossless matching network $\mathbf{Z}^\mathrm{MT}$ transmuting the impedance of uncoupled multi-port generator R to the optimum generator impedance $\mathbf{Z}_\mathrm{G}$.

We now derive the network $\mathbf{Z}^\mathrm{MT}$ in detail. The $\mathbf{Z}^\mathrm{MT}$ interfaces individual generators to the transmitting-side of the antenna system, which is described as

$$\begin{bmatrix}\mathbf{u}_1\\ \mathbf{u}_\mathrm{t}\end{bmatrix} = \mathbf{Z}^\mathrm{MT}\begin{bmatrix}\mathbf{i}_1\\ -\mathbf{i}_\mathrm{t}\end{bmatrix}. \tag{6}$$

For *a reciprocal, lossless and linear* network, we have

$$\mathbf{Z}^\mathrm{MT} = \mathrm{j}\begin{bmatrix}X_{11}^\mathrm{MT} & X_{12}^\mathrm{MT}\\ X_{21}^\mathrm{MT} & X_{22}^\mathrm{MT}\end{bmatrix}. \tag{7}$$

with $\mathrm{j} = \sqrt{-1}$. From Fig. 3, the voltage $\mathbf{u}_\mathrm{t}$ and the current $\mathbf{i}_\mathrm{t}$ are related to the input impedance by,

$$\mathbf{u}_\mathrm{t} = \mathbf{Z}_\mathrm{G}^\dagger \mathbf{i}_\mathrm{t}. \tag{8}$$

Substituting (8) and the decoupling condition (5) into (6), we obtain

$$R\mathbf{I}\mathbf{i}_1 = \left\{\mathrm{j}X_{11}^\mathrm{MT} + X_{12}^\mathrm{MT}(\mathbf{Z}_\mathrm{G}^\dagger + \mathrm{j}X_{22}^\mathrm{MT})^{-1}X_{21}^\mathrm{MT}\right\}\mathbf{i}_1, \tag{9}$$

or, more explicitly,

$$R\mathbf{I} = \mathrm{j}X_{11}^\mathrm{MT} + X_{12}^\mathrm{MT}\left(\mathrm{Re}\{\mathbf{Z}_\mathrm{G}^\dagger\} + \mathrm{j}\mathrm{Im}\{\mathbf{Z}_\mathrm{G}^\dagger\} + \mathrm{j}X_{22}^\mathrm{MT}\right)^{-1} X_{21}^\mathrm{MT}. \tag{10}$$

Relation (10) has many solutions, which lead to different possible $\mathbf{Z}^\mathrm{MT}$ designs. One such network design is of the form [19]

$$\mathbf{Z}^\mathrm{MT} = \mathrm{j}\begin{bmatrix}\mathbf{0} & \sqrt{R}\left(\mathrm{Re}\{\mathbf{Z}_\mathrm{G}^\dagger\}\right)^{1/2}\\ \sqrt{R}\left(\mathrm{Re}\{\mathbf{Z}_\mathrm{G}^\dagger\}\right)^{1/2} & -\mathrm{Im}\{\mathbf{Z}_\mathrm{G}^\dagger\}\end{bmatrix}. \tag{11}$$

Moreover looking at the generator side of Fig. 3, voltage $\mathbf{u}_1$ is given by,

$$\mathbf{u}_1 = \mathbf{u}_\mathrm{G} - R\mathbf{i}_1, \tag{12}$$

so that, together with (6) and (11), it can be shown that

$$\mathbf{i}_\mathrm{t} = \frac{\mathrm{j}}{2\sqrt{R}}\left(\mathrm{Re}\{\mathbf{Z}_\mathrm{G}^\dagger\}\right)^{-1/2}\mathbf{u}_\mathrm{G}. \tag{13}$$

Substituting (13) into (1) and also considering the fact that $\mathbf{u}_\mathrm{R} = -\mathbf{Z}_\mathrm{L}\mathbf{i}_\mathrm{R}$, it can be shown that

$$\mathbf{i}_\mathrm{r} = -\frac{\mathrm{j}}{2\sqrt{R}}\left(\mathbf{Z}_\mathrm{L} + \mathbf{Z}_{22}\right)^{-1}\mathbf{Z}_{21}\left(\mathrm{Re}\{\mathbf{Z}_\mathrm{G}^\dagger\}\right)^{-1/2}\mathbf{u}_\mathrm{G}. \tag{14}$$

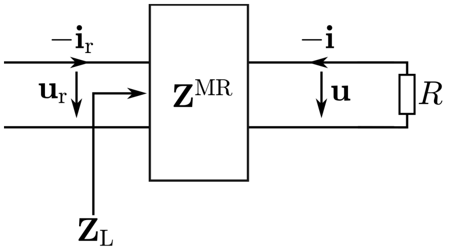

Fig. 4. Block diagram of the matching network $\mathbf{Z}^\mathrm{MR}$ transmuting the uncoupled load impedances R to the optimum load impedance $\mathbf{Z}_\mathrm{L}$.

Likewise, in order to obtain the optimum load impedance from the uncoupled multiple load resistances, we introduce another *linear, reciprocal and lossless* Matching network on the Receiver-side (MR) with impedance parameter denoted by $\mathbf{Z}^\mathrm{MR}$, as illustrated in Fig. 4, defined as

$$\begin{bmatrix}\mathbf{u}_\mathrm{r}\\ \mathbf{u}\end{bmatrix} = \mathbf{Z}^\mathrm{MR}\begin{bmatrix}-\mathbf{i}_\mathrm{r}\\ -\mathbf{i}\end{bmatrix}. \tag{15}$$

By following a similar procedure such as to obtain (11), one can attain a Matching network for the Receiver side ($\mathbf{Z}^\mathrm{MR}$) as

$$\mathbf{Z}^\mathrm{MR} = \mathrm{j}\begin{bmatrix}-\mathrm{Im}\{\mathbf{Z}_\mathrm{L}^\dagger\} & -\sqrt{R}\left(\mathrm{Re}\{\mathbf{Z}_\mathrm{L}^\dagger\}\right)^{1/2}\\ -\sqrt{R}\left(\mathrm{Re}\{\mathbf{Z}_\mathrm{L}^\dagger\}\right)^{1/2} & \mathbf{0}\end{bmatrix}. \tag{16}$$

By substituting (14) into (15), it can be shown that the voltages at the receiver side, $\mathbf{u}$, are related to the voltages at the generator side, $\mathbf{u}_\mathrm{G}$, by

$$\mathbf{u} = \boldsymbol{\mathcal{H}}\frac{\mathbf{u}_\mathrm{G}}{2}, \tag{17}$$

where

$$\boldsymbol{\mathcal{H}} = \left(\mathrm{Re}\{\mathbf{Z}_\mathrm{L}^\dagger\}\right)^{1/2}\left(\mathbf{Z}_\mathrm{L} + \mathbf{Z}_{22}\right)^{-1}\mathbf{Z}_{21}\left(\mathrm{Re}\{\mathbf{Z}_\mathrm{G}^\dagger\}\right)^{-1/2}. \tag{18}$$

Note that the matrix $\boldsymbol{\mathcal{H}}$ relates the *end-to-end* voltages and is a complex dimensionless $L \times L$ matrix.

B. Equally Strong Parallel Multi-Channel Communication

In the previous section, we have described a procedure to obtain the maximum transmission between the transmitter and receiver by performing a power-matching condition, which is achieved by solving (4) using the iterative scheme described in Appendix A. The end-to-end voltages are related by the dimensionless matrix $\boldsymbol{\mathcal{H}}$, which is consistent with the *channel matrix* in the information theoretic model [16], [18]. In this section, we describe a procedure to obtain conditions for equally strong orthogonal multi-channel communication.

It is important to note that because of the network matching and decoupling procedure described above, the channel matrix $\boldsymbol{\mathcal{H}}$ provides the optimum channel, which ensures maximum power transfer from the independent generators to the receiver load. The transmitted power P_T and received power P_R can be calculated as

$$P_T = \frac{\mathbf{u}_\mathrm{G}^\dagger\mathbf{u}_\mathrm{G}}{4R} \quad \text{and} \quad P_R = \frac{\mathbf{u}^\dagger\mathbf{u}}{R} = \frac{\mathbf{u}_\mathrm{G}^\dagger\boldsymbol{\mathcal{H}}^\dagger\boldsymbol{\mathcal{H}}\mathbf{u}_\mathrm{G}}{4R}. \tag{19}$$

Therefore, *channel power gain* defined as

$$G = \max\frac{P_R}{P_T} \tag{20}$$

is related to the channel matrix $\mathcal{H}$ as

$$G = \max_{\text{eigval}}\{\mathcal{H}^{\dagger}\mathcal{H}\}. \tag{21}$$

Note that the channel matrix described here has an equal number L of transmitting and receiving antennas, such that the system can support a maximum of L independent channels. To investigate these independent channels, we perform a singular-value decomposition on $\mathcal{H}$,

$$\mathcal{H} = \mathbf{U}\Sigma\mathbf{V}^{\dagger}, \tag{22}$$

where

$$\mathbf{U}\mathbf{U}^{\dagger} = \mathbf{U}^{\dagger}\mathbf{U} = \mathbf{I} \quad \text{and } \mathbf{V}\mathbf{V}^{\dagger} = \mathbf{V}^{\dagger}\mathbf{V} = \mathbf{I} \tag{23}$$

are two unitary matrices whose individual columns form an orthonormal basis of both the transmitted and received signal. The matrix Σ is a diagonal matrix which comprises all the singular values of the channel matrix $\mathcal{H}$. That is,

$$\Sigma = \begin{bmatrix} s_1 & & & \\ & s_2 & & \\ & & \ddots & \\ & & & s_L \end{bmatrix}. \tag{24}$$

These singular values are nonnegative and are assumed to be ordered as

$$s_1 \geq s_2 \geq \cdots \geq s_L. \tag{25}$$

Applying (22)-(25) to calculate $\mathcal{H}^{\dagger}\mathcal{H}$, it can be shown that s_i^2 are the eigenvalues of $\mathcal{H}^{\dagger}\mathcal{H}$ and the columns of $\mathbf{V}$ are the eigenvectors of $\mathcal{H}^{\dagger}\mathcal{H}$. Thus the channel gain (21) is

$$G = s_1^2. \tag{26}$$

For clarity, we would like to emphasise that in this paper the term *channel gain* is reserved for the maximum eigenvalue of $\mathcal{H}^{\dagger}\mathcal{H}$, as in (21); we refer to a generic eigenvalue s_i^2 as the *channel strength* of channel i.

A maximum number L of independent (orthogonal) channels can be established by linear signal processing, such that, adopting from information theory, we can define the system of communication channels as

$$\boldsymbol{y} = \mathcal{H}\boldsymbol{x}, \tag{27}$$

where the *channel input* $\boldsymbol{x}$ and *channel output* $\boldsymbol{y}$ are defined naturally such that,

$$\mathrm{E}[\boldsymbol{x}^{\dagger}\boldsymbol{x}] = P_T \quad \text{and } \mathrm{E}[\boldsymbol{y}^{\dagger}\boldsymbol{y}] = P_R. \tag{28}$$

That is, the expectation value $(\mathrm{E}[\cdot])$ of the channel-input $\boldsymbol{x}$ and channel-output $\boldsymbol{y}$ correspond to the transmitted and received powers, respectively. Thus, the channel-input and channel-output are given by the following mappings,

$$\boldsymbol{x} = \mathbf{V}^{\dagger}\frac{\mathbf{u}_{\mathrm{G}}}{2\sqrt{R}} \quad \text{and } \boldsymbol{y} = \mathbf{U}^{\dagger}\frac{\mathbf{u}}{\sqrt{R}} \tag{29}$$

respectively. Therefore, following the information theoretic model, by substituting (23) and (24) into (29), it can be shown that the channel output component can be expressed as

$$y_i = s_i x_i, \tag{30}$$

where x_i and y_i denote the component of $\boldsymbol{x}$ and $\boldsymbol{y}$, respectively.

Ideally, it is desirable that all the L available channels have the *same strength* which requires one to fine-tune the antenna system such that all the eigenvalues are roughly the same [29]. That is

$$s_1^2 \approx s_2^2 \approx \cdots \approx s_L^2. \tag{31}$$

Hence, a channel matrix fulfilling condition (31) defines a setting for a multichannel communication with L non-interfering and equally strong channels.

Up to now, we have not considered noise. Next, we will study the impact of noise assuming the presence of: (i) *thermal equilibrium noise* arising from the antenna system and the generator at the transmit-side and (ii) *non-equilibrium noise* produced by the receive amplifiers. The $\mathbf{Z}^{\mathrm{MR}}$ presents decoupled ports of resistance R to the receiver's amplifiers. Thus the open-circuit noise voltage $\mathbf{u}_{\mathrm{N}}$ of these ports has the covariance matrix,

$$\mathrm{E}[\mathbf{u}_{\mathrm{N}}\mathbf{u}_{\mathrm{N}}^{\dagger}] = 4k_{\mathrm{B}}TBR\mathbf{I}, \tag{32}$$

where k_{B} is Boltzmann's constant, T is temperature in Kelvin, B is bandwidth and $\mathbf{I}$ is an identity matrix of size $L \times L$.

Equation (32) is valid under the assumption that the white thermal equilibrium noise at the receiver is the result of the port decoupling process of the DMNs. Moreover, the non-equilibrium noise of the amplifiers is also white, provided that the physical noise sources of the amplifiers are pairwise uncorrelated between different amplifiers. Therefore, the noise contribution of the individual amplifiers *do not* mix with each other. As a consequence, the total noise (sum of equilibrium and non-equilibrium noise) is pairwise uncorrelated in the components of the received voltage vector $\mathbf{u}$. From (23), it follows that $\boldsymbol{y}$ contains pairwise uncorrelated noise components. Therefore, (30) can be extended to include the effect of combined thermal equilibrium noise of the antenna and the non-equilibrium noise of the receive amplifiers as,

$$y_i = s_i x_i + \nu_i, \quad i \in \{1, 2, \cdots, L\}, \tag{33}$$

where the correlation of noises ν_i is given by

$$\mathrm{E}[\nu_i \nu_j^*] = \sigma_v^2 \delta_{ij}. \tag{34}$$

In (34), δ_{ij} is the Kronecker delta function which equals 1 for $i = j$ and zero otherwise. In the case that the noises ν_i are Gaussian distributed, they are also pairwise independent.

III. CASE WITH 2 × 2 MIMO DIPOLE ANTENNAS

In the previous section, we have presented the procedures involved in optimising a MIMO set-up for near-field communication making use of *Decoupling and Matching Networks* (DMNs). Furthermore, we also described the condition required to achieve L non-interfering and equally strong communication channels in this regime. In this section, we demonstrate the procedure for a 2×2 MIMO antenna system using dipole antennas and discuss the conditions for the existence of equally strong orthogonal communication channels in the near-field regime. The importance of the decoupling and matching process in acquiring these channels will be shown.

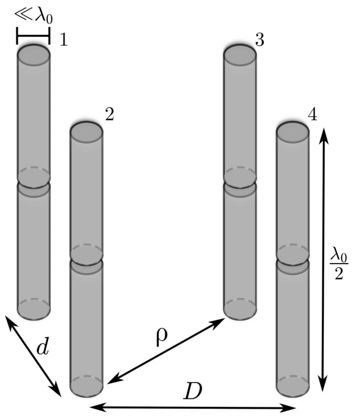

Fig. 5. A 2 × 2 half-wavelength infinitesimally thin dipole antennae. The transmitters (antenna 1 & 2) and receivers (antenna 3 & 4) are separated by distance D. Distance d separates the transmitter (or receiver) antennas.

Fig. 5 illustrates the set of four half-wavelength dipole antennas in free-space considered in this section. The choice of half-wavelength dipole antennas is taken because the self/mutual impedances are well-described by the induced EMF (iEMF) model [28], [30] then allowing for a semi-analytical study of the effect. For consistency, the transmitter is labeled as antennas 1 and 2; the receiver as antennas 3 and 4. The distance d denotes the separation between the transmitter (or receiver) antennas and distance D denotes the separation between the transmitter and receiver side; we will refer to d as *intra-separation* and D as *inter-separation*. For the antenna configuration illustrated in Fig. 5, the antenna system impedance in the iEMF approximation is given by,

$$\mathbf{Z} = \begin{bmatrix} Z_{\mathrm{s}} & Z(d) & Z(D) & Z(\rho) \\ Z(d) & Z_{\mathrm{s}} & Z(\rho) & Z(D) \\ Z(D) & Z(\rho) & Z_{\mathrm{s}} & Z(d) \\ Z(\rho) & Z(D) & Z(d) & Z_{\mathrm{s}} \end{bmatrix}, \tag{35}$$

where the diagonal and off-diagonal entries in (35) denote the self-impedance and the mutual-impedance respectively and are defined by the resistance and admittance parameter as,

$$Z(r) = R_{\mathrm{A}}(r) + \mathrm{j}X_{\mathrm{A}}(r), \tag{36}$$

where r is the distance between the dipole pairs.

For *half-wavelength (total length) dipole antennas*, assuming an infinitesimally thin wire radius and sinusoidal profile of surface current, the mutual impedance between two antenna elements is given by, (see Appendix B),

$$\begin{aligned} R_{\mathrm{A}}(r \neq 0) &= \frac{2\mathrm{Ci}(\frac{2\pi r}{\lambda_0}) - \mathrm{Ci}(\xi + \pi) - \mathrm{Ci}(\xi - \pi)}{4\pi\varepsilon_0 c}, \\ X_{\mathrm{A}}(r \neq 0) &= \frac{-2\mathrm{Si}(\frac{2\pi r}{\lambda_0}) + \mathrm{Si}(\xi + \pi) + \mathrm{Si}(\xi - \pi)}{4\pi\varepsilon_0 c}, \end{aligned} \tag{37}$$

with

$$\xi = \pi\sqrt{1 + 4r^2/\lambda_0^2} \tag{38}$$

and the self-impedance is obtained as

$$R_{\mathrm{A,s}} = \frac{\Gamma - \mathrm{Ci}(2\pi) + \ln(2\pi)}{4\pi\varepsilon_0 c}, \quad X_{\mathrm{A,s}} = \frac{\mathrm{Si}(2\pi)}{4\pi\varepsilon_0 c}. \tag{39}$$

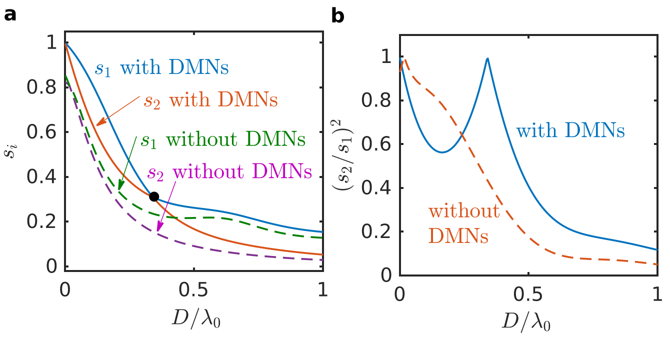

Fig. 6. (a) The two eigenvalues of $\boldsymbol{\mathcal{H}}^{\dagger}\boldsymbol{\mathcal{H}}$ and (b) the ratio of the two eigenvalues s_2^2/s_1^2. For the case when the DMNs are present (solid-lines) and absent (dashed-lines) and $d = 0.25\lambda_0$.

In (37) and (39), Ci(·) and Si(·) denote the cosine and sine integral functions [31]. The constants ε and Γ are the vacuum electric permittivity and Euler constant, respectively.

A. Multi-Channel Dipole-Based MIMO Communication

Upon obtaining the antenna impedance parameter $\mathbf{Z}$ from (35), we perform the network optimization numerically, see Appendix A, to find the optimum load impedances $\mathbf{Z}_{\mathrm{L}}$ and generator multi-port impedances $\mathbf{Z}_{\mathrm{G}}$ from which the channel matrix $\boldsymbol{\mathcal{H}}$ is calculated. For the 2 × 2 antenna system we consider here, there exists two usable communication channels whose *strength* is represented by the eigenvalues s_i^2, where $i \in \{1, 2\}$. These eigenvalues are presented in Fig. 6(a) as a function of the inter-separation distance D. For comparison, the eigenvalues for the case *without* DMNs are also presented by dashed lines.

Fig. 6(a) shows that the presence of the DMNs increases the strength of all available communication channels compared to when the DMNs are not implemented. Although results for different d are not shown in this paper, in general the presence of DMNs enhances the channel strength compared to when the DMNs are not implemented. It is noted here that, although in general the channel strength decreases as the inter-separation distance D increases, in the presence of DMNs there exists a specific distance D at which the two singular values cross, marked with a black bullet point in Fig. 6(a); this indicates a configuration for which *a non-interfering two-channel communication with equally strong channels* is established.

Fig. 6(a) depicts the channel strengths, s_i^2, and is useful to determine the quality of each communication channel. However, to find equally strong channels, the ratio of the two eigenvalues s_2^2/s_1^2 shown in Fig. 6(b) is more informative. To have good multi-channel communication, it is desired to have channels with equal gain, that is $s_2^2/s_1^2 \approx 1$ which is fulfilled around $D = 0.34\lambda_0$, see Fig. 6(b). Moreover, since s_2^2/s_1^2 can also be interpreted as the ratio of the power gain of the second-best channel, Fig. 6 emphasises the role of the DMNs in increasing the strength of the second channel relative to the first, i.e. in lessening the disparity of between the two channels.

The results in Fig. 6 are for a specific intra-separation distance $d = 0.25\lambda_0$ and this leads to an optimal separation

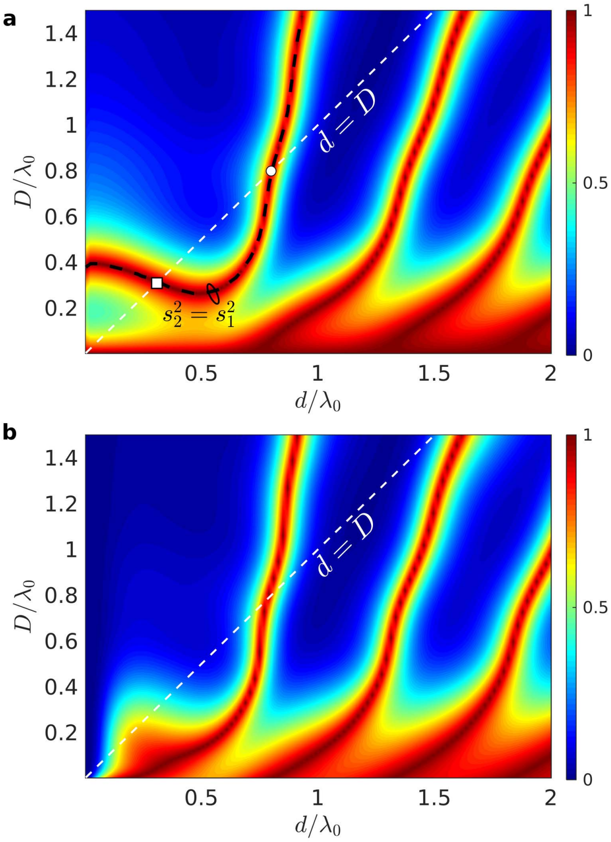

Fig. 7. The ratio of the two eigenvalues s_2^2/s_1^2 as a function of D and d, when the DMNs are (a) present and (b) *absent*.

distance $D = 0.34\lambda_0$ where the two channels have the same eigenvalues, $s_1^2 = s_2^2$. We note that this optimal separation point depends on both D and d as shown in Fig. 7(a). Fig. 7 depicts the distribution of s_2^2/s_1^2 as a function of distance d and D for two different conditions: (a) for the case when the DMNs are present and (b) for the case when the DMNs are absent.

Inspection of Fig. 7(a) and Fig. 7(b) shows that the presence of the DMNs significantly modifies the channel strengths in the near-field while they have less influence in the far-field. This corroborates the role of the DMNs, which is to provide a matching condition in the near-field regime which is critical due to the strong coupling (mutual-impedance) between adjacent antennas. More importantly, Fig. 7(a) shows that the DMNs allow the creation of channels with equal strength ($s_1^2 = s_2^2$) in the extreme near-field region, i.e. $D < 0.4\lambda_0$ and $d < 0.4\lambda_0$, whereas this is *not* the case when the DMNs are *absent*, see Fig. 7(b).

We now turn our attention to the black dashed line in Fig. 7(a). This line corresponds to optimum operation at which the two channels have the same strength, $s_1^2 = s_2^2$. Since along this line the channel matrix has equal singular values, the channel power gain coincides with the channel strength. This is presented in Fig. 8. For reference, we have included square (□) and circle bullets (◯) denoting the case when $d = D$, see also Fig. 7. From Fig. 8, the maximum channel power gain G is achieved when the intra-separation distance is

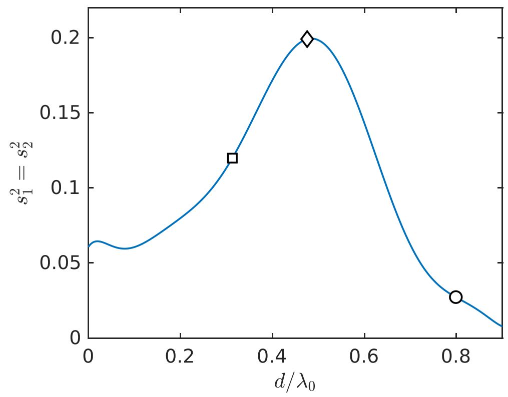

Fig. 8. The eigenvalues $s_{1,2}$ of $\boldsymbol{\mathcal{H}}^\dagger\boldsymbol{\mathcal{H}}$ when two equally strong orthogonal channels are established; i.e. the black-dashed-line in Fig. 7.

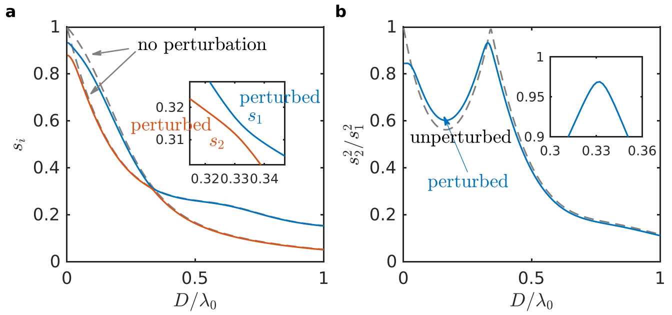

Fig. 9. Impact of antenna imperfection to the channel communication performance. In (a) the two singular values of $\boldsymbol{\mathcal{H}}$ and (b) the ratio of the two eigenvalues s_2^2/s_1^2. For reference, the unperturbed case, i.e. all the four antennas are identical, are presented as dashed lines. The insets show enlarged view for clarity. Intra-separation distance $d = 0.25\lambda_0$.

$d = 0.474\lambda_0$, marked by the diamond bullet (◊); at this point the channel power gain is $G = s_1^2 = 0.2025$; this signifies that about 20% of the transmitted power can be received. In practice, however, we are interested in the case of $d \leq D$. Thus the maximum achievable received power gain is at a distance $d = 0.313\lambda_0$ with about 12%, i.e. $G = s_1^2 = 0.1175$.

B. System Robustness

For the configuration considered so far, we have assumed that all the antennas are identical and that we have equal values for the self-impedance (diagonal entries of $\mathbf{Z}$) for all antennas. In practice, antennas are prone to fabrication errors, such that it is difficult to construct antennas with an identical specification which leads to slight differences in the self-impedance.

We note that the communication channel is sensitive to these antenna imperfections. To demonstrate this, we perturb the self-impedance of our dipole antenna, i.e. the diagonal entries of $\mathbf{Z}$, by introducing slight differences in the antenna lengths. For the sake of clarity, the channel strength for $\ell_1 = 0.498\lambda_0$, $\ell_2 = 0.503\lambda_0$, $\ell_3 = 0.502\lambda_0$ and $\ell_4 = 0.501\lambda_0$ is shown in Fig. 9, where ℓ_i denotes the length of dipole i. Here, the intra-separation distance is fixed at $d = 0.25\lambda_0$. From Fig. 9(a) it can be seen that the two eigenvalues avoid a crossing when the antennas are *not* identical. The optimal operation point $s_2^2/s_1^2 = 1$ is thus unattainable in practice, see Fig. 9(b).

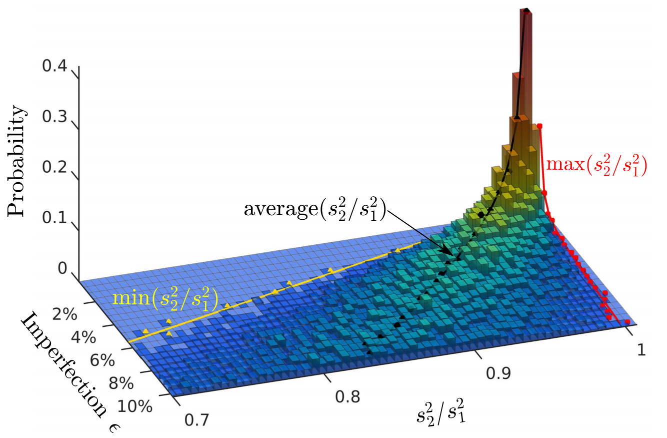

Fig. 10. The probability distribution of the peak of s_2^2/s_1^2 as the function of imperfection parameter ϵ. The maximum, average and minimum values of s_2^2/s_1^2 are plotted as bullet point with red, black and yellow color respectively, fitted-lines are included for reference.

To elaborate on this, Fig. 10 shows the probability distribution of the peak of s_2^2/s_1^2 as a function of the imperfection parameter ϵ which *randomly* perturbs the length of the dipole. This random perturbation is produced by $\ell \leftarrow 0.5\lambda_0(1+\epsilon\delta)$, where $\delta \sim \mathcal{N}(0, 0.3)$ with $\mathcal{N}(0, 0.3)$, a normally distributed random number generator centered at zero with variance 0.3. The probability distribution in Fig. 10 is obtained by performing 1000 different realizations of the MIMO system. Fig. 10 further shows that the probability of achieving an equally strong orthogonal channel diminishes in the presence of self-impedance perturbation. Data-fitting of $\max(s_2^2/s_1^2)$ shows that the probability of achieving $(s_2^2/s_1^2) = 1$ decreases in an exponential rate as the imperfection ϵ increases.

C. Comparison With Full-Wave FDTD Simulation

In previous sections, the antenna impedance was obtained by an iEMF model which is based on a thin wire approximation and makes simplifying assumptions about the current profile in the wire, hence neglecting the influence of nearby antennas.

For comparison, we perform here a full-wave numerical simulation using a commercially available Finite-Difference Time-Domain (FDTD) software suit, EMPIRE XPU™ [32]. We obtain the self and mutual impedances of the MIMO antenna system and compare these to the results obtained from the iEMF model described in the previous sections. The full-wave FDTD method simulates the same antenna configuration as in Sec. III-A, but now as a physical system with a well-defined radius of the wire of the dipole antenna, here set at $a = 0.02\lambda_0$. Furthermore, the FDTD simulation introduces spatial-meshing and time-stepping; we apply a graded-mesh scheme with maximum mesh parameters of the size $\lambda_0/25$ and at least five discretisation points on the thin wire structure. The (self and mutual) impedance parameters obtained from the FDTD simulation are presented in Fig. 11. For reference, Fig. 11 also includes the impedances calculated from the iEMF method, i.e. (39) and (37), in which self-impedences are independent of the distance D.

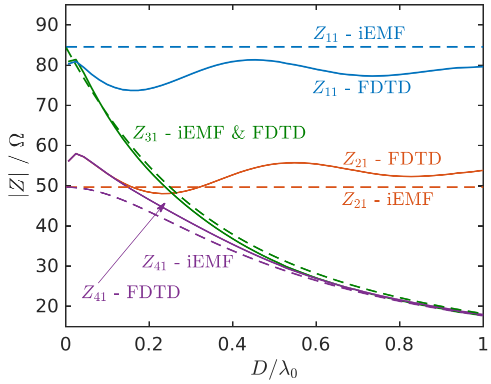

Fig. 11. Impedance parameters of the MIMO antenna system, obtained by the induced EMF model (dashed lines) and the full-wave FDTD simulations (solid lines).

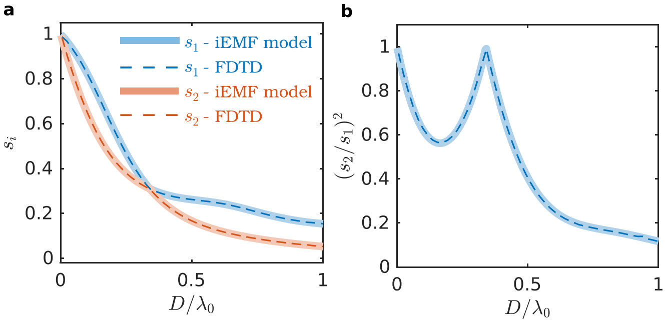

Fig. 12. (a) The two singular values of $\boldsymbol{\mathcal{H}}$ and (b) the ratio of the two eigenvalues s_2^2/s_1^2 calculated by the FDTD method. For comparison, the results obtained from the iEMF model, i.e. Fig. 6, are included.

In general, the FDTD and iEMF model show good agreement for the mutual-impedance parameters of the system, see Fig. 11. Difference in the impedance parameters is mainly due to the assumptions in the iEMF model, namely of an *idealised* sinusoidal profile of surface current on an *infinitesimally* thin wire which neglects any perturbation caused by the presence of nearby antennas [28], [30]. This is affirmed by Fig. 11, which shows the increase of the deviation as the distance D decreases; consistent with [33], which notes a similar behaviour of the impedance parameters in near-field region.

Similarly to the procedure applied in Sec. III-A but now using the antenna impedance obtained from the FDTD simulation, we perform the power matching procedure to obtain the optimum load impedances $\mathbf{Z}_{\mathrm{L}}$ and generator multiport impedances $\mathbf{Z}_{\mathrm{G}}$ numerically, see Appendix A. From these, the channel matrix $\boldsymbol{\mathcal{H}}$ is calculated. The channel strengths, s_i^2, are depicted in Fig. 12 as a function of distance D. For comparison, the results which are obtained using the antenna impedance from the iEMF model, i.e. from Fig. 6, are reproduced again in Fig. 12.

It is interesting to note that, despite the difference in the impedance parameters, the channel strength obtained from the iEMF impedance agrees with the one based on the FDTD simulation, see Fig. 12. The rationale of this counter-intuitive behaviour is that the network optimisation finds the required DMNs in order to achieve the optimum power transmission. This affirms the importance of network optimisation in finding the optimal possible decoupling and matching networks (DMNs) necessary in order to attain the highest possible transmission.

IV. CONCLUSION AND OUTLOOK

A systematic procedure for obtaining an optimum transmission with equally strong multi-channel MIMO in the near-field is presented. The optimisation procedure includes: (i) a decoupling and matching process maximizing the power transmitted and received by the MIMO system, and (ii) finding equally strong orthogonal multi-channel operation by evaluating the individual channel power gains. The proposed optimization process is applied to a 2×2 dipole antenna configuration. Using this configuration, we identify the existence of equally strong orthogonal two-channel modes of operation with optimal transmission (up to 12% power gain for operation at $d = D = 0.313\lambda_0$) in the near-field region; this is only possible if the network optimization has been performed. Our calculation shows the important characteristic that for MIMO communication in the near-field the optimum power density is achieved *only* at particular locations (*not directions*); suggesting that the optimisation procedure described in this paper is different to beamforming-type optimisation.

While results are not included in this paper, our calculation shows that further improvement in the power gain transmission can be obtained by increasing the number of antennas in a linear array. We also note that high quality antennas with consistent specification are necessary in order to achieve this optimum transmission. Furthermore we find that the DMNs are successful in obtaining the highest possible transmission in the presence of strong inter-antenna coupling.

Finally, we envisage that the main disturbance in the near-field communication links will, to a large extent, stem from electromagnetic interference produced by processing information and control signals surrounding the analogue propagation channels of the near-field communication links; this is in addition to the *weak* interuser interference in multipoint communication systems. The dominant electromagnetic interference is independent of the presence other near-field communication links; it is *different* to the usual multi-user interference in wireless communications. Our initial investigations [34]–[37] show that noise in the near-field is highly correlated, which is different from the thermal equilibrium noise. We see the circuit model for information channel described in this paper is fundamental in the investigation of MIMO communication in a noisy near-field environment.

APPENDIX A
NUMERICAL PROCEDURE TO CALCULATE THE OPTIMUM LOAD AND GENERATOR MULTIPORT IMPEDANCES IN (4)

Determines the optimum load and generator multiport impedances $\mathbf{Z}_\mathrm{L}$ and $\mathbf{Z}_\mathrm{G}$ which ensure maximum power transfer from the transmitter to the receiver.

In Algorithm 1, α is a random scalar number generated from a uniform random number generator $\alpha \sim \mathcal{U}(0.1, 0.9)$. The conditional statement, $||\cdot||_\mathrm{F} < \mathrm{tol}$, is the Frobenius matrix norm for a preset tolerance, tol.

Algorithm 1 Iterative Solver for Optimum Load and Generator Multiport Impedances

```
Let $\mathbf{Z}_\mathrm{L} \leftarrow \mathbf{Z}_{22}^\dagger$
Compute $\mathbf{Z}_\mathrm{in} = \mathbf{Z}_{11} - \mathbf{Z}_{12}(\mathbf{Z}_{22} + \mathbf{Z}_\mathrm{L})^{-1}\mathbf{Z}_{21}$ and
$\mathbf{Z}_\mathrm{out} = \mathbf{Z}_{22} - \mathbf{Z}_{21}(\mathbf{Z}_{11} + \mathbf{Z}_\mathrm{G})^{-1}\mathbf{Z}_{12}$.
while $||\mathbf{Z}_\mathrm{out}^\dagger - \mathbf{Z}_\mathrm{L}||_\mathrm{F} \geq \mathrm{tol}$ do
    $\mathbf{Z}_\mathrm{L} \leftarrow \alpha\mathbf{Z}_\mathrm{L} + (1-\alpha)\mathbf{Z}_\mathrm{out}^\dagger$
    $\mathbf{Z}_\mathrm{in} = \mathbf{Z}_{11} - \mathbf{Z}_{12}(\mathbf{Z}_{22} + \mathbf{Z}_\mathrm{L})^{-1}\mathbf{Z}_{21}$
    $\mathbf{Z}_\mathrm{G} \leftarrow \mathbf{Z}_\mathrm{in}^\dagger$
    $\mathbf{Z}_\mathrm{out} = \mathbf{Z}_{22} - \mathbf{Z}_{21}(\mathbf{Z}_{11} + \mathbf{Z}_\mathrm{G})^{-1}\mathbf{Z}_{12}$.
end while
$\mathbf{Z}_\mathrm{G} \leftarrow \mathbf{Z}_\mathrm{in}^\dagger$
```

APPENDIX B
THE SELF/MUTUAL IMPEDANCE OF DIPOLE LENGTH ℓ BY THE INDUCED EMF MODEL

The self-impedance ($Z_\mathrm{s} = R_\mathrm{s} + \mathrm{j}X_\mathrm{s}$) of an infinitesimally thin-wire dipole antenna that has an arbitrary total length ℓ operated at $k_0 = 2\pi/\lambda_0$, is given by the induced EMF (iEMF) model as [30],

$$\begin{aligned} R_{\mathrm{A,s}}(\ell) &= \frac{1}{2\pi\varepsilon_0 c} \\ &\Big\{\Gamma + \ln(k_0\ell) - \mathrm{Ci}(k_0\ell) + \frac{1}{2}\sin(k_0\ell)\left[\mathrm{Si}(2k_0\ell) - 2\mathrm{Si}(k_0\ell)\right] \\ &+ \frac{1}{2}\cos(k_0\ell)\left[\Gamma + \ln(k_0\ell/2) + \mathrm{Ci}(k_0\ell) - 2\mathrm{Ci}(k_0\ell)\right]\Big\}, \qquad (40) \end{aligned}$$

$$\begin{aligned} X_{\mathrm{A,s}}(\ell) &= \frac{1}{4\pi\varepsilon_0 c}\left\{2\mathrm{Si}(k_0\ell) + \cos(k_0\ell)\left[2\mathrm{Si}(k_0\ell) - \mathrm{Si}(2k_0\ell)\right]\right. \\ &\left. + \sin(k_0\ell)\left[2\mathrm{Ci}(k_0\ell) - \mathrm{Ci}(2k_0\ell) - 2\mathrm{Ci}\left(\frac{2k_0a^2}{\ell}\right)\right]\right\}. \qquad (41) \end{aligned}$$

The mutual-impedance ($Z(r) = R_\mathrm{A}(r) + \mathrm{j}X_\mathrm{A}(r)$), on the other hand, is highly dependent on the distance r between the antennas while depending weakly on ℓ. The resistance and the admittance are given by,

$$R_\mathrm{A}(r \neq 0) = \frac{1}{4\pi\varepsilon_0 c}\left\{2\mathrm{Ci}(u_0) - \mathrm{Ci}(u_1) - \mathrm{Ci}(u_2)\right\} \qquad (42)$$

$$X_\mathrm{A}(r \neq 0) = -\frac{1}{4\pi\varepsilon_0 c}\left\{2\mathrm{Si}(u_0) - \mathrm{Si}(u_1) - \mathrm{Si}(u_2)\right\} \qquad (43)$$

where the arguments in (43) are given by,

$$\begin{aligned} u_0 &= k_0 r, \\ u_1 &= k_0(\sqrt{r^2 + \ell^2} + \ell), \\ u_2 &= k_0(\sqrt{r^2 + \ell^2} - \ell). \qquad (44) \end{aligned}$$

In (40) to (43), the functions $\mathrm{Ci}(\cdot)$ and $\mathrm{Si}(\cdot)$ denote the cosine and sine integral function [31]. The constant ε_0, c and Γ is the vacuum electric permittivity, speed-of-light in vacuum and Euler constant, respectively. For the specific case of half-wavelength dipole antenna $\ell = \lambda_0/2$, the self and mutual impedance are given in the main text as (37) and (39).

ACKNOWLEDGMENT

The support of IMST GmbH for access to the EMPIRE XPU™ is greatly acknowledge. Authors would like to thank to

Peter Russer, David W.P. Thomas, Steve Greedy, Johannes Russer and Mohamed Ismaeel Maricar for many valuable discussion.

REFERENCES

[1] SIA/SRC. (2015). *Rebooting the IT Revolution: A Call to Action*. [Online]. Available: https://www.semiconductors.org/clientuploads/Resources/RITR%20WEB%20version%20FINAL.pdf

[2] D. A. B. Miller and H. M. Ozaktas, "Limit to the bit-rate capacity of electrical interconnects from the aspect ratio of the system architecture," *J. Parallel Distrib. Comput.*, vol. 41, pp. 42–52, Feb. 1997.

[3] D. A. B. Miller, "Device requirements for optical interconnects to silicon chips," *Proc. IEEE*, vol. 97, no. 7, pp. 1166–1185, Jul. 2009.

[4] J. A. Davis *et al.*, "Interconnect limits on gigascale integration (GSI) in the 21st century," *Proc. IEEE*, vol. 89, no. 3, pp. 305–324, Mar. 2001.

[5] I. P. Kaminow, T. Li, and A. E. Willner, *Optical Fiber Telecommunications Volume B: Systems and Networks*. Amsterdam, The Netherlands: Elsevier, 2008.

[6] M. F. Chang, V. P. Roychowdhury, L. Zhang, H. Shin, and Y. Qian, "RF/wireless interconnect for inter- and intra-chip communications," *Proc. IEEE*, vol. 89, no. 4, pp. 456–466, Apr. 2001.

[7] Nemf21. Accessed: Aug. 31, 2017. [Online]. Available: http://www.nemf21.org/

[8] R. K. Kostuk, J. W. Goodman, and L. Hesselink, "Optical imaging applied to microelectronic chip-to-chip interconnections," *Appl. Opt.*, vol. 24, no. 17, pp. 2851–2858, 1985.

[9] F. Deicke, W.-J. Fisher, and M. Faulwaßer, "Optical wireless communication to eco-system," in *Proc. IEEE Future Netw. Mobile Summit (FutureNetw)*, Jul. 2012, pp. 1–8.

[10] K.-D. Langer and J. Grubor, "Recent developments in optical wireless communications using infrared and visible light," in *Proc. 9th Int. Conf. Transp. Opt. Netw. (ICTON)*, vol. 3. Jul. 2007, pp. 146–151.

[11] K. K. O *et al.*, "On-chip antennas in silicon ICs and their application," *IEEE Trans. Electron Devices*, vol. 52, no. 7, pp. 1312–1323, Jul. 2005.

[12] Y. Zheng, Y. Zhang, and Y. Tong, "A novel wireless interconnect technology using impulse radio for interchip communications," *IEEE Trans. Microw. Theory Techn.*, vol. 54, no. 4, pp. 1912–1920, Jun. 2006.

[13] Z. M. Chen and Y. P. Zhang, "Inter-chip wireless communication channel: Measurement, characterization, and modeling," *IEEE Trans. Antennas Propag.*, vol. 55, no. 3, pp. 978–986, Mar. 2007.

[14] M. I. Maricar *et al.*, "Analysis of a near field MIMO wireless channel using 5.6 GHz dipole antennas," in *Proc. ESA Workshop Aerosp. EMC (Aerospace EMC)*, May 2016, pp. 1–3.

[15] J. H. Winters, "On the capacity of radio communication systems with diversity in a Rayleigh fading environment," *IEEE J. Sel. Areas Commun.*, vol. SAC-5, no. 5, pp. 871–878, Jun. 1987.

[16] G. J. Foschini and M. J. Gans, "On limits of wireless communications in a fading environment when using multiple antennas," *Wireless Pers. Commun.*, vol. 6, no. 3, pp. 311–335, Mar. 1998.

[17] G. C. Raleigh and J. M. Cioffi, "Spatio-temporal coding for wireless communication," *IEEE Trans. Commun.*, vol. 46, no. 3, pp. 357–366, Mar. 1998.

[18] M. T. Ivrlač and J. A. Nossek, "The multiport communication theory," *IEEE Circuits Syst. Mag.*, vol. 14, no. 3, pp. 27–44, 3rd Quart., 2014.

[19] M. T. Ivrlač and J. A. Nossek, "Toward a circuit theory of communication," *IEEE Trans. Circuits Syst. I, Reg. Papers*, vol. 57, no. 7, pp. 1663–1683, Jul. 2010.

[20] M. T. Ivrlač and J. A. Nossek, "High-efficiency super-gain antenna arrays," in *Proc. ITG Int. Workshop Smart Antennas*, Bremen, Germany, Feb. 2010, pp. 369–374.

[21] M. T. Ivrlač and J. A. Nossek, "On the diversity performance of compact antenna arrays," in *Proc. 30th Gen. Assembly Int. Union Radio Sci. (URSI)*, Istanbul, Turkey, Aug. 2011, pp. 1–4. [Online]. Available: http://www.ursi.org/proceedings/procGA11/ursi/DBC-1.pdf

[22] M. T. Ivrlač and J. A. Nossek, "On multistreaming with compact antenna arrays," in *Proc. ITG Int. Workshop Smart Antennas*, Aachen, Germany, Feb. 2011, pp. 1–8.

[23] M. T. Ivrlač and J. A. Nossek, "On the physical meaning of the model of two uncoupled isotrops," in *Proc. ITG Workshop Smart Antennas (WSA)*, Dresden, Germany, Mar. 2012, pp. 256–263.

[24] M. T. Ivrlač and J. A. Nossek, "Gaussian multiple access channel with compact antenna arrays," in *Proc. IEEE Symp. Inf. Theory (ISIT)*, Saint Petersburg, Russia, Jul. 2001, pp. 728–731.

[25] M. T. Ivrlač and J. A. Nossek, "Physical modeling of communication systems in information theory," in *Proc. IEEE Int. Symp. Inf. Theory (ISIT)*, Seoul, South Korea, Jun. 2009, pp. 2179–2183.

[26] M. T. Ivrlač and J. A. Nossek, "Quantifying diversity and correlation in Rayleigh fading MIMO communication systems," in *Proc. 3rd IEEE Int. Symp. Signal Process. Inf. Technol. (ISSPIT)*, Dec. 2003, pp. 158–161.

[27] Y. Fei, Y. Fan, B. K. Lau, and J. S. Thompson, "Optimal single-port matching impedance for capacity maximization in compact MIMO arrays," *IEEE Trans. Antennas Propag.*, vol. 56, no. 11, pp. 3566–3575, Nov. 2008.

[28] S. J. Orfanidis. *Electromagnetic Waves and Antennas*. Accessed: Aug. 31, 2017. [Online]. Available: http://www.ece.rutgers.edu/~orfanidi/ewa/

[29] M. T. Ivrlač, *Wireless MIMO Systems—Models, Performance, Optimization*. Aachen, Germany: Shaker, 2005.

[30] C. A. Balanis, *Antenna Theory: Analysis and Design*, 3rd ed. Hoboken, NJ, USA: Wiley, 2005.

[31] M. Abramowitz and I. A. Stegun, *Handbook of Mathematical Functions: With Formulas, Graphs, and Mathematical Tables*. New York, NY, USA: Dover, 1972.

[32] IMST GmbH. *EMPIRE XPU—FDTD Simulator for 3D EM Modeling of Antennas, Filters, Multilayer Components, Packages, Waveguide Elements, RCS, EMC and SAR Calculations*. Accessed: Aug. 31, 2017. [Online]. Available: http://www.empire.de/

[33] J. W. Wallace and M. A. Jensen, "Mutual coupling in MIMO wireless systems: A rigorous network theory analysis," *IEEE Trans. Wireless Commun.*, vol. 3, no. 4, pp. 1317–1325, Jul. 2004.

[34] G. Gradoni *et al.*, "Wigner-function-based propagation of stochastic field emissions from planar electromagnetic sources," *IEEE Trans. Electromagn. Compat.*, vol. 60, no. 3, pp. 580–588, Jun. 2018.

[35] J. A. Russer *et al.*, "Correlation measurement and evaluation of stochastic electromagnetic fields," in *Proc. Int. Symp. Electromagn. Compat.-EMC (EUROPE)*, Sep. 2016, pp. 12–16.

[36] Y. Kuznetsov *et al.*, "Localization of the equivalent sources on the PCB surface by using ultra-wideband time domain near-field measurements," in *Proc. Int. Symp. Electromagn. Compat.-EMC (EUROPE)*, Sep. 2016, pp. 1–6.

[37] J. A. Russer *et al.*, "Evolution of transverse correlation in stochastic electromagnetic fields," in *IEEE MTT-S Int. Microw. Symp. Dig.*, May 2015, pp. 1–3.

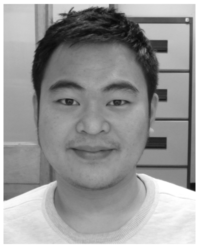

Sendy Phang received the B.Eng. degree (Hons.) in engineering physics from the Bandung Institute of Technology, Bandung, Indonesia, in 2010, and the M.Sc. degree in electromagnetic design and the Ph.D. degree in electrical and electronic engineering from the University of Nottingham, Nottingham, U.K., in 2011 and 2016, respectively. Since 2016, he has been a Research Fellow with the School of Mathematical Sciences, University of Nottingham. His research interests include the application of electromagnetic (EM) theory for periodic structures, parity-time symmetric structure in photonics, and topological EM structure. He was a recipient of the 2017 Young Scientist Award presented by the URSI General Assembly.

Michel T. Ivrlač received the first Dipl.-Ing. degree in electrical engineering from the Munich University of Applied Sciences, in 1994, and the second Dipl.-Ing. degree and the Dr.-Ing. degree in electrical engineering and information technology from the Technische Universität München (TUM) in 1998 and 2005, respectively. He currently holds the position of a Senior Researcher with the Institute for Circuit Theory and Signal Processing, TUM, where he is also teaching courses on circuit theory and communication. His main research interests are the physics of communications, signal processing for cellular networks, and coding for ultrahigh speed communications.

Gabriele Gradoni (M'11) received the Ph.D. degree in electromagnetics from the Università Politecnica Delle Marche, Ancona, Italy, in 2010. In 2008, he was a Visiting Researcher with the Time, Quantum & Electromagnetics Team, National Physical Laboratory, Teddington, U.K. From 2010 to 2013, he was a Research Associate with the Institute for Research in Electronics and Applied Physics, University of Maryland, College Park, MD, USA. From 2013 to 2016, he was a Research Fellow with the School of Mathematical Sciences, University of Nottingham, U.K. Since 2016, he has been an Assistant Professor of mathematics and electrical engineering with the University of Nottingham. His research activity is in probabilistic and asymptotics methods for propagation in complex wave systems, wave chaos, and MIMO wireless systems. He is a member of the American Physical Society and the Italian Electromagnetics Society. He was a recipient of the URSI Commission B Young Scientist Award in 2010 and 2016, and the Gaetano Latmiral Prize in 2015. Since 2014, he has been the URSI Commission E Early Career Representative.

Stephen C. Creagh received the B.Sc. degree in physics from the National University of Ireland, University College Cork in 1986 and the Ph.D. degree in physics from the University of California at Berkeley, Berkeley, CA, USA, in 1991. He was a Post-Doctoral Researcher with the Niels Bohr Institute, Denmark, University of Regensburg, Germany, Université de Paris Sud, Orsay, France, and CEA Saclay, France, before joining the University of Nottingham, U.K. in 1998, where he is currently an Associate Professor with the School of Mathematical Sciences. His research interests include the use of semiclassical and short-wave asymptotic methods to understand the response of chaotic and complex wave systems, including EM, acoustic, and quantum problems.

Gregor Tanner received the Diploma in physics in 1989 and the Ph.D. degree in theoretical physics in 1992 - both from the University of Freiburg, Germany. From 1994 to 1996, he was a Post-Doctoral Fellow with the Niels Bohr Institute, Copenhagen, Denmark, and from 1996 to 1998, he was a Research Fellow with the Hewlett Packard Laboratories, Bristol, U.K. He joined the School of Mathematical Sciences, University of Nottingham, U.K., as a Lecturer in 1998 and became a Reader and a Professor of Applied Mathematics in 2004 and 2016, respectively.

Josef A. Nossek (S'72–M'74–SM'81–F'93–LF'13) received the Dipl.-Ing. and Dr. techn. degrees in electrical engineering from the Vienna University of Technology, Austria, in 1974 and 1980, respectively. He joined Siemens AG, Germany, in 1974, where he was engaged in filter design for communication systems. From 1987 to 1989, he was the Head of the Radio Systems Design Department, where he was instrumental in introducing high-speed VLSI signal processing into digital microwave radio. From 1989 to 2016, he was the Head of the Institute of Circuit Theory and Signal Processing (NWS), Technical University Munich, Germany. In 2016, he joined the Universidade Federal do Ceara, Fortaleza, Brasil, as a Full Professor. He was the President Elect, the President, and the Past President of the IEEE Circuits and Systems Society in 2001, 2002, and 2003, respectively. He was the President of Verband der Elektrotechnik, Elektronik, und Informationstechnik (VDE) from 2007 to 2008 and the President of the Convention of National Associations of Electrical Engineers of Europe in 2013. He was a recipient of the ITG Best Paper Award in 1988, the Mannesmann Mobilfunk (currently Vodafone) Innovations Award in 1998, and the Award for Excellence in Teaching from the Bavarian Ministry for Science, Research and Art in 1998. From the IEEE Circuits and Systems Society, he received the Golden Jubilee Medal for Outstanding Contributions to the Society in 1999 and the Education Award in 2008. He received the Order of Merit of the Federal Republic of Germany (Bundesverdienstkreuz am Bande) in 2008. In 2011, he received the IEEE Guillemin-Cauer Best Paper Award and in 2013 the honorary doctorate (Dr. h. c.) from the Peter Pazmany Catholic University, Hungary. He received the VDE Ring of Honor in 2014 and the TUM Emeritus of Excellence in 2016. In 2009, he became a member of the National Academy of Engineering in Germany (acatech).